Progress In Electromagnetics Research, Vol. 136, 607–622, 2013

STRUCTURE ANALYSIS OF SINGLE- AND MULTI-FREQUENCY SUBSPACE MIGRATIONS IN INVERSE SCATTERING PROBLEMS

Young-Deuk Joh, Young Mi Kwon, Joo Young Huh, and Won-Kwang Park*

Department of Mathematics, Kookmin University, Seoul 136-702, Korea

Abstract—We carefully investigate the structure of single- and multi-frequency imaging functions, that are usually employed in inverse scattering problems. Based on patterns of the singular vectors of the Multi-Static Response (MSR) matrix, we establish a relationship between imaging functions and the Bessel function. This relationship indicates certain properties of imaging functions and the reason behind enhancement in the imaging performance by multiple frequencies. Several numerical simulations with a large amount of noisy data are performed in order to support our investigation.

1. INTRODUCTION

One of the main objectives of the inverse scattering problem is to identify the characteristics of unknown targets from measured scattered field or far-field pattern. In research fields such as physics, medical science, and materials engineering, this is an interesting and important problem. Related works can be found in [2, 7, 9–11, 32] and references therein. In order to solve this problem, various algorithms for finding the locations and/or shapes of targets have been accordingly developed.

In many research studies [1, 7, 9, 13, 17, 26], the shape reconstruction method is based on Newton-type iterative algorithms. However, for a successful shape reconstruction using these algorithms, the iterative procedure must begin with a good initial guess that is close to the unknown target because it highly depends on the initial guess; for more details, refer to [16, 26].

Received 3 December 2012, Accepted 21 January 2013, Scheduled 24 January 2013

* Corresponding author: Won-Kwang Park (parkwk@kookmin.ac.kr).

To find a good initial guess, alternative non-iterative reconstruction algorithms have been developed, such as the MUltiple SIgnal Classification (MUSIC)-type algorithm [5, 23, 25], linear sampling method [8, 12], topological derivative strategy [3, 6, 18, 21, 22], linear-δ, vector and multipolarized approaches [29, 30], and the multi-frequency based algorithm such as Kirchhoff and subspace migrations [2, 4, 15, 19, 20, 24]. Among them, although the multi-frequency based subspace migration has exhibited potential as a non-iterative imaging technique, a mathematical identification of its structure needs to be performed for its heuristical applications, which is the motivation behind.

In this paper, by intensively analyzing the structure of single- and multi-frequency subspace migration, we discover some properties and confirm the reason behind the enhancement in the imaging performance by applying multiple frequencies. In recent work [4], this fact was verified by the Statistical Hypothesis Testing but our approach is to find a relationship between imaging functions and Bessel functions of the first kind of the integer order.

This paper is organized as follows. In Section 2, we briefly review the two-dimensional direct scattering problem, and an asymptotic expansion formula for far-field patterns, and introduce the imaging function introduced in [19]. In Section 3, we analyze the single- and multi-frequency based imaging functions and discuss their properties. In Section 4, we present several numerical experiments and discuss the effectiveness, robustness, and limitation of imaging functions. Finally, a brief conclusion is given in Section 5.

2. REVIEW ON IMAGING FUNCTION

In this section, we survey the two-dimensional direct scattering problem and an imaging algorithm. A more detailed discussion can be found in [4, 5, 19, 20, 24].

2.1. Direct Scattering Problem and Asymptotic Expansion Formula

Let Σ_m be a homogeneous inclusion with a small diameter ρ in the two-dimensional space $\mathbb{R}^2$. Throughout this paper, we assume that every Σ_m is expressed as

$$\Sigma_m = \mathbf{r}_m + \rho\mathcal{D}_m,$$

where $\mathbf{r}_m$ and ρ denote the location and size of Σ_m, respectively. Here, $\mathcal{D}_m$ is a simple connected smooth domain containing the origin.

Let ε_0 and μ_0 respectively denote the dielectric permittivity and magnetic permeability of $\mathbb{R}^2$. Similarly, we let ε_m and μ_m be those of Σ_m. For simplicity, let Σ be the collection of Σ_m, $m = 1, 2, \ldots, M$, and we define the following piecewise constants:

$$\varepsilon(\mathbf{r}) = \begin{cases} \varepsilon_m & \text{for} \quad \mathbf{r} \in \Sigma_m \\ \varepsilon_0 & \text{for} \quad \mathbf{r} \in \mathbb{R}^2 \backslash \bar{\Sigma} \end{cases} \quad \text{and} \quad \mu(\mathbf{r}) = \begin{cases} \mu_m & \text{for} \quad \mathbf{r} \in \Sigma_m \\ \mu_0 & \text{for} \quad \mathbf{r} \in \mathbb{R}^2 \backslash \bar{\Sigma}. \end{cases}$$

Throughout this paper, we assume that $\varepsilon_0 = \mu_0 = 1$ and $\varepsilon_m > \varepsilon_0$, $\mu_m > \mu_0$ for $m = 1, 2, \ldots, M$. At a given frequency ω, let $u_{\text{tot}}(\mathbf{r}, \mathbf{d}_l; \omega)$ be the time-harmonic total field that satisfies the Helmholtz equation

$$\nabla \cdot \left(\frac{1}{\mu(\mathbf{r})} \nabla u_{\text{tot}}(\mathbf{r}, \mathbf{d}_l; \omega) \right) + \omega^2 \varepsilon(\mathbf{r}) u_{\text{tot}}(\mathbf{r}, \mathbf{d}_l; \omega) = 0 \tag{1}$$

with transmission conditions at the boundaries of Σ_m.

Let $u_{\text{inc}}(\mathbf{r}, \mathbf{d}_l; \omega)$ be the solution of (1) without Σ. In this paper, we consider the following plane-wave illumination: for a vector $\mathbf{d}_l \in \mathfrak{C}^1$, $u_{\text{inc}}(\mathbf{r}, \mathbf{d}_l; \omega) = \exp(j\omega \mathbf{d}_l \cdot \mathbf{r})$. Here, $\mathfrak{C}^1$ denotes the unit circle in $\mathbb{R}^2$.

Generally, the total field u_{tot} can be divided into the incident field u_{inc} and the unknown scattered field u_{scat}, which satisfies the Sommerfeld radiation condition

$$\lim_{|\mathbf{r}| \to \infty} \sqrt{|\mathbf{r}|} \left(\frac{\partial u_{\text{scat}}(\mathbf{r}, \mathbf{d}_l; \omega)}{\partial |\mathbf{r}|} - jk_0 u_{\text{scat}}(\mathbf{r}, \mathbf{d}_l; \omega) \right) = 0,$$

uniformly in all directions $\hat{\mathbf{r}} = \frac{\mathbf{r}}{|\mathbf{r}|}$. Since we assumed $\varepsilon_0 = \mu_0 = 1$, wavenumber k_0 satisfies $k_0 = \omega\sqrt{\varepsilon_0 \mu_0} = \omega$. As given in [5], u_{scat} can be written as the following asymptotic expansion formula

$$\begin{aligned} u_{\text{scat}}(\mathbf{r}, \mathbf{d}_l; \omega) = &\rho^2 \sum_{m=1}^{M} \Big(\nabla u_{\text{inc}}(\mathbf{r}_m, \mathbf{d}_l; \omega) \cdot \mathbb{T}(\mathbf{r}_m) \cdot \nabla \Phi(\mathbf{r}_m, \mathbf{r}, \omega) \\ &+ \omega^2 (\varepsilon - \varepsilon_0) \text{area}(\mathcal{D}_m) u_{\text{inc}}(\mathbf{r}_m, \mathbf{d}_l; \omega) \Phi(\mathbf{r}_m, \mathbf{r}, \omega) \Big) + o(\rho^2), \end{aligned} \tag{2}$$

where $o(\rho^2)$ is uniform in $\mathbf{r}_m \in \Sigma_m$ and $\mathbf{d}_l \in \mathfrak{C}^1$. Here $\text{area}(\mathcal{D}_m)$ denotes the area of $\mathcal{D}_m$, $\mathbb{T}(\mathbf{r}_m)$ is a 2×2 symmetric matrix:

$$\mathbb{T}(\mathbf{r}_m) = \frac{2\mu_0}{\mu_m + \mu_0} \text{area}(\mathcal{D}_m) \mathbb{I}_2,$$

where $\mathbb{I}_n$ denotes the $n \times n$ identity matrix, and $\Phi(\mathbf{r}_m, \mathbf{r}, \omega)$ is the two-dimensional time harmonic Green function

$$\Phi(\mathbf{r}_m, \mathbf{r}, \omega) = -\mu_0 \frac{j}{4} H_0^1(\omega |\mathbf{r}_m - \mathbf{r}|),$$

where H_0^1 is the Hankel function of order zero and of the first kind.

The far-field pattern is defined as function $F(\hat{\mathbf{r}},\mathbf{d}_l)$ that satisfies

$$u_{\text{scat}}(\mathbf{r},\mathbf{d}_l;\omega)=\frac{\exp(jk_0|\mathbf{r}|)}{\sqrt{|\mathbf{r}|}}F(\hat{\mathbf{r}},\mathbf{d}_l)+o\left(\frac{1}{\sqrt{|\mathbf{r}|}}\right) \tag{3}$$

as $|\mathbf{r}|\to\infty$ uniformly on $\hat{\mathbf{r}}=\frac{\mathbf{r}}{|\mathbf{r}|}$.

2.2. Introduction to Subspace Migration

The imaging algorithm introduced in [19] used the structure of a singular vector of the Multi-Static Response (MSR) matrix $\mathbb{M}=(F_{pq})=(F(\hat{\mathbf{r}}_p,\mathbf{d}_q))_{p,q=1}^{N}$, whose elements $F(\hat{\mathbf{r}}_p,\mathbf{d}_q)$ is (3) with observation number p and incident number q. Note that by combining (2), (3), and the asymptotic behavior of the Hankel function, the far-field pattern $F(\hat{\mathbf{r}}_p,\mathbf{d}_q)$ can be represented as the asymptotic expansion formula (see [5] for instance)

$$\begin{aligned}F(\hat{\mathbf{r}}_p,\mathbf{d}_q)\approx\rho^2\frac{\omega^2(1+j)}{4\sqrt{\omega\pi}}\sum_{m=1}^{M}\left(\frac{\varepsilon-\varepsilon_0}{\sqrt{\varepsilon_0\mu_0}}\text{area}(\mathcal{D}_m)-\hat{\mathbf{r}}_p\cdot\mathbb{T}(\mathbf{r}_m)\cdot\mathbf{d}_q\right)\\ \times\exp\Big(jk_0(\mathbf{d}_q-\hat{\mathbf{r}}_p)\cdot\mathbf{r}_m\Big).\end{aligned} \tag{4}$$

For the sake of simplicity, we eliminate the constant $\frac{\omega^2(1+j)}{4\sqrt{\omega\pi}}$ in (4). Then, the incident and observation direction configurations are kept same, i.e., for each $\hat{\mathbf{r}}_p=-\mathbf{d}_p$, the pq-th element of the MSR matrix $\mathbb{M}$ is given by

$$\begin{aligned}F_{pq}\;=\;F(\hat{\mathbf{r}}_p,\mathbf{d}_q)\Big|_{\hat{\mathbf{r}}_p=-\mathbf{d}_p}&\approx\rho^2\sum_{m=1}^{M}\left[\frac{\varepsilon_m-\varepsilon_0}{\sqrt{\varepsilon_0\mu_0}}\text{area}(\mathcal{D}_m)\right.\\ &\left.+\frac{2\mu_0}{\mu_m+\mu_0}\text{area}(\mathcal{D}_m)\mathbf{d}_p\cdot\mathbf{d}_q\right]\exp\Big(jk_0(\mathbf{d}_p+\mathbf{d}_q)\cdot\mathbf{r}_m\Big).\end{aligned}$$

Based on the above representation of F_{pq}, we introduce a vector $\mathbf{D}(\mathbf{r};\omega)\in\mathbb{C}^{N\times3}$ as

$$\mathbf{D}(\mathbf{r};\omega):=\begin{pmatrix}\mathbf{e}_1\exp(jk_0\mathbf{d}_1\cdot\mathbf{r})\\ \mathbf{e}_2\exp(jk_0\mathbf{d}_2\cdot\mathbf{r})\\ \vdots\\ \mathbf{e}_N\exp(jk_0\mathbf{d}_N\cdot\mathbf{r})\end{pmatrix},\quad\text{where}\quad\mathbf{e}_p=(1,\mathbf{d}_p)^T. \tag{5}$$

Then $\mathbb{M}$ can be decomposed as follows:

$$\mathbb{M}=\sum_{m=1}^{M}\mathbf{D}(\mathbf{r}_m;\omega)\begin{pmatrix}\rho^2\frac{\varepsilon_m-\varepsilon_0}{\sqrt{\varepsilon_0\mu_0}}\text{area}(\mathcal{D}_m) & \mathbb{O}_{1\times2}\\ \mathbb{O}_{2\times1} & \rho^2\mathbb{T}(\mathbf{r}_m)\end{pmatrix}\mathbf{D}(\mathbf{r}_m;\omega)^T,$$

where $\mathbb{O}_{p\times q}$ denotes the $p \times q$ zero matrix. This decomposition leads us to introduce an imaging algorithm as follows. First, let us perform the Singular Value Decomposition (SVD) as follows:

$$\mathbb{M} = \mathbb{U}\mathbb{S}\bar{\mathbb{V}}^T = \sum_{m=1}^{M} \sigma_m(\omega)\mathbf{U}_m(\omega)\bar{\mathbf{V}}_m(\omega)^T, \tag{6}$$

where $\mathbf{U}_m$ and $\mathbf{V}_m$ are the left and right singular vectors, respectively, and $\bar{a}$ denotes the complex conjugate of a. Then, based on the structure of (5), we define a vector $\hat{\mathbf{D}}(\mathbf{r};\omega) \in \mathbb{C}^{N\times 1}$:

$$\hat{\mathbf{D}}(\mathbf{r};\omega) := \begin{pmatrix} \mathbf{c}\cdot(1,\mathbf{d}_1)^T \exp(jk_0\mathbf{d}_1\cdot\mathbf{r}) \\ \mathbf{c}\cdot(1,\mathbf{d}_2)^T \exp(jk_0\mathbf{d}_2\cdot\mathbf{r}) \\ \vdots \\ \mathbf{c}\cdot(1,\mathbf{d}_N)^T \exp(jk_0\mathbf{d}_N\cdot\mathbf{r}) \end{pmatrix}, \quad \mathbf{c} \in \mathbb{C}^{3\times 1}\backslash\{\mathbf{0}\}, \tag{7}$$

and corresponding unit vector

$$\mathbf{W}(\mathbf{r};\omega) := \frac{\hat{\mathbf{D}}(\mathbf{r};\omega)}{|\hat{\mathbf{D}}(\mathbf{r};\omega)|}. \tag{8}$$

With this, we can introduce a subspace migration as follows

$$\mathbb{W}(\mathbf{r};\omega) := \left|\sum_{m=1}^{M}\left(\bar{\mathbf{W}}(\mathbf{r};\omega)\cdot\mathbf{U}_m(\omega)\right)\left(\bar{\mathbf{W}}(\mathbf{r};\omega)\cdot\bar{\mathbf{V}}_m(\omega)\right)\right|. \tag{9}$$

Note that since the first M columns of the matrices $\{\mathbf{U}_1,\ \mathbf{U}_2,\ \ldots,\ \mathbf{U}_M\}$ and $\{\mathbf{V}_1,\ \mathbf{V}_2,\ \ldots,\ \mathbf{V}_M\}$ are orthonormal, we can observe that

$$\begin{aligned} &\bar{\mathbf{W}}(\mathbf{r};\omega)\cdot\mathbf{U}_m(\omega)\approx 1 \quad \text{and} \quad \bar{\mathbf{W}}(\mathbf{r};\omega)\cdot\bar{\mathbf{V}}_m(\omega)\approx 1 \quad \text{if} \quad \mathbf{r}=\mathbf{r}_m \\ &\bar{\mathbf{W}}(\mathbf{r};\omega)\cdot\mathbf{U}_m(\omega)\approx 0 \quad \text{and} \quad \bar{\mathbf{W}}(\mathbf{r};\omega)\cdot\bar{\mathbf{V}}_m(\omega)\approx 0 \quad \text{if} \quad \mathbf{r}\neq\mathbf{r}_m, \end{aligned}$$

for $m = 1,\ 2,\ \ldots,\ M$. Therefore, $\mathbb{W}(\mathbf{r};\ \omega)$ will plots peaks of magnitude of 1 at $\mathbf{r} = \mathbf{r}_m \in \Sigma_m$, and of small magnitude at $\mathbf{r} \notin \Sigma_m$ (see [4, 19, 20, 24]). Complete algorithm is summarized in Algorithm 1.

3. STRUCTURE ANALYSIS OF IMAGING FUNCTIONS

3.1. Structure of Single-frequency Subspace Migration (9)

We now determine the structure of imaging function (9). Before proceeding, we assume that scatterers are well resolved by the measurement array and based on the Rayleigh resolution limit from far-field data, any detail less than one-half of the wavelength cannot be seen so that scatterers are well-separated to each other, refer to [2].

Algorithm 1 Imaging algorithm via Subspace Migration (SM)

```
procedure SM($\omega$)
    identify permittivity $\varepsilon_0$ and permeability $\mu_0$ of $\mathbb{R}^2$
    given $\omega$, initialize $\mathbb{W}(\mathbf{r};\omega)$
    for $q = 1$ to $N$ do
        for $p = 1$ to $N$ do
            collect MSR matrix data $F(\hat{\mathbf{r}}_p, \mathbf{d}_q) \in \mathbb{M}$        ▷ see (4)
        end for
    end for
    perform SVD of $\mathbb{M} = \mathbb{U}\mathbb{S}\overline{\mathbb{V}}^T$        ▷ see (6)
    choose $\{\mathbf{U}_1, \mathbf{U}_2, \ldots, \mathbf{U}_M\}$ and $\{\mathbf{V}_1, \mathbf{V}_2, \ldots, \mathbf{V}_M\}$        ▷ see [25]
    for $\mathbf{r} \in \Omega \subset \mathbb{R}^2$ do        ▷ $\Omega$ is a search domain
        generate $\hat{\mathbf{D}}(\mathbf{r};\omega)$ and $\mathbf{W}(\mathbf{r};\omega)$        ▷ see (7) and (8)
        initialize $I(\mathbf{r})$
        for $m = 1$ to $M$ do
            $I(\mathbf{r}) \leftarrow I(\mathbf{r}) + (\overline{\mathbf{W}}(\mathbf{r};\omega) \cdot \mathbf{U}_m(\omega))(\overline{\mathbf{W}}(\mathbf{r};\omega) \cdot \overline{\mathbf{V}}_m(\omega))$
        end for
        $\mathbb{W}(\mathbf{r};\omega) = |I(\mathbf{r})|$
    end for        ▷ see (9)
    plot $\mathbb{W}(\mathbf{r};\omega)$ and find $\mathbf{r} = \mathbf{r}_m \in \Sigma_m$        ▷ $\mathbb{W}(\mathbf{r};\omega) \approx 1$
end procedure
```

For determining the structure, we recall some useful statements.

Lemma 3.1 ([4]). *A relation $A \sim B$ means that there exists a constant C such that $A = CB$. Then, for vectors $\mathbf{U}_m$ and $\mathbf{V}_m$ in (6) and $\mathbf{W}(\mathbf{r};\omega)$ in (8), the following relationship holds*

$$\mathbf{W}(\mathbf{r}_m;\omega) \sim \mathbf{U}_m(\omega) \quad \text{and} \quad \mathbf{W}(\mathbf{r}_m;\omega) \sim \bar{\mathbf{V}}_m(\omega).$$

Lemma 3.2 ([14]). *Let $\mathbf{d}, \mathbf{r} \in \mathbb{R}^2$, and $\omega > 0$; then*

$$\int_{\mathfrak{S}^1} \exp(j\omega \mathbf{d} \cdot \mathbf{r}) dS(\mathbf{d}) = 2\pi J_0(\omega|\mathbf{r}|),$$

where $J_\nu(x)$ denotes the Bessel function of order ν of the first kind.

Subsequently, we can explore the structure of (9) as follows

Lemma 3.3. *If the total number of incident and observation directions N is sufficiently large and satisfies $N > M$, then the imaging function (9) can be represented as follows*:

$$\mathbb{W}(\mathbf{r};\omega) \sim \sum_{m=1}^{M} J_0(\omega|\mathbf{r}_m - \mathbf{r}|)^2. \tag{10}$$

Proof. By hypothesis, we assume that N is sufficiently large. Since the incident and observation direction configurations are same, we set

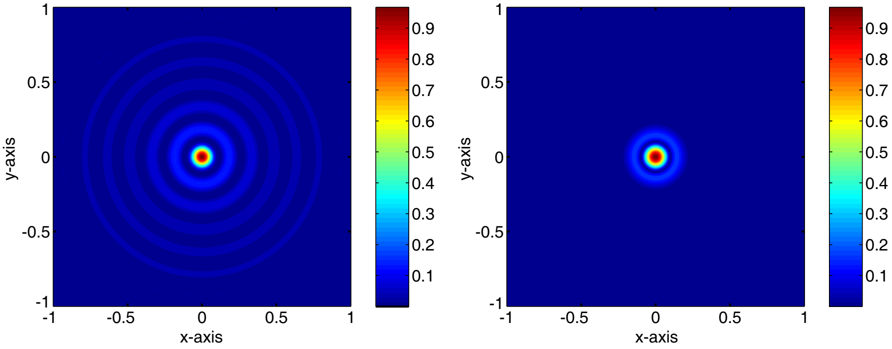

(a) (b)

Figure 1. (a) 2-D plot of (10) for $\omega = \frac{2\pi}{0.3}$ and (b) 2-D plot of (11) for $\omega_1 = \frac{2\pi}{0.5}$ and $\omega_S = \frac{2\pi}{0.3}$ when $m = 1$ and $\mathbf{r}_m = \mathbf{0}$.

$\triangle\mathbf{d}_p := |\mathbf{d}_p - \mathbf{d}_{p-1}|$ for $p = 2, 3, \ldots, N$, and $\triangle\mathbf{d}_1 := |\mathbf{d}_1 - \mathbf{d}_N|$. Then, applying Lemmas 3.1 and 3.2 yields

$$\begin{aligned}
\mathbb{W}(\mathbf{r};\omega) &= \left|\sum_{m=1}^{M}\Big(\bar{\mathbf{W}}(\mathbf{r};\omega)\cdot\mathbf{U}_m(\omega)\Big)\Big(\bar{\mathbf{W}}(\mathbf{r};\omega)\cdot\bar{\mathbf{V}}_m(\omega)\Big)\right| \\
&\sim \sum_{m=1}^{M}\left(\sum_{p=1}^{N}\exp(j\omega\mathbf{d}_p\cdot(\mathbf{r}_m-\mathbf{r}))\frac{\triangle\mathbf{d}_p}{2\pi}\right)^2 \\
&\approx \frac{1}{4\pi^2}\sum_{m=1}^{M}\left(\int_{\mathfrak{S}^1}\exp(j\omega\mathbf{d}\cdot(\mathbf{r}_m-\mathbf{r}))dS(\mathbf{d})\right)^2=\sum_{m=1}^{M}J_0(\omega|\mathbf{r}_m-\mathbf{r}|)^2.
\end{aligned}$$

This completes the proof.

Note that $J_0(x)$ has the maximum value 1 at $x = 0$. This is the reason that the map of $\mathbb{W}(\mathbf{r};\,\omega)$ plots magnitude 1 at $\mathbf{r} = \mathbf{r}_m \in \Sigma_m$. Moreover, due to the oscillating property of $J_0(x)$, Theorem 3.3 indicates why imaging function (9) plots unexpected replicas, as shown in Figure 1.

3.2. Reason Behind Enhancement in the Imaging Performance by Applying Multiple Frequencies

According to Theorem 3.3, the oscillating pattern of the Bessel function must be reduced or eliminated in order to improve the imaging performance. One way to do so is to apply the high-frequency $\omega = +\infty$ in theory. Another way is to apply several frequencies to the imaging function (9) as follows:

$$\begin{aligned}\mathbb{W}(\mathbf{r};S) :=& \frac{1}{S}\left|\sum_{s=1}^{S}\mathbb{W}(\mathbf{r};\omega_s)\right|\\ =& \frac{1}{S}\left|\sum_{s=1}^{S}\sum_{m=1}^{M}\Big(\bar{\mathbf{W}}(\mathbf{r};\omega_s)\cdot\mathbf{U}_m(\omega_s)\Big)\Big(\bar{\mathbf{W}}(\mathbf{r};\omega_s)\cdot\bar{\mathbf{V}}_m(\omega_s)\Big)\right|. \quad (11)\end{aligned}$$

Several researches in [2, 4, 19, 20] have confirmed on the basis of Statistical Hypothesis Testing and numerical experiments that the multi-frequency imaging function (11) is an improved version of the single-frequency version (10). The reason for this is discussed as follows.

Theorem 3.4 *If ω_S and the total number of incident and observation directions N is sufficiently large and satisfies $N > M$, then the structure of the imaging function (11) is*

$$\begin{aligned}\mathbb{W}(\mathbf{r};S) \sim \sum_{m=1}^{M}\Bigg[&\frac{\omega_S}{\omega_S-\omega_1}\Big(J_0(\omega_S|\mathbf{r}_m-\mathbf{r}|)^2+J_1(\omega_S|\mathbf{r}_m-\mathbf{r}|)^2\Big)\\ &-\frac{\omega_1}{\omega_S-\omega_1}\Big(J_0(\omega_1|\mathbf{r}_m-\mathbf{r}|)^2+J_1(\omega_1|\mathbf{r}_m-\mathbf{r}|)^2\Big)\Bigg]. \quad (12)\end{aligned}$$

Proof. According to (10), we can observe that

$$\mathbb{W}(\mathbf{r};S) \approx \frac{1}{S}\sum_{s=1}^{S}\sum_{m=1}^{M}J_0(\omega_s|\mathbf{r}_m-\mathbf{r}|)^2 \approx \sum_{m=1}^{M}\int_{\omega_1}^{\omega_S}\frac{J_0(\omega|\mathbf{r}_m-\mathbf{r}|)^2}{\omega_S-\omega_1}d\omega.$$

Using this, we apply an indefinite integral formula of the Bessel function (see [27, page 35]):

$$\int J_0(x)^2dx = x\Big(J_0(x)^2+J_1(x)^2\Big)+\int J_1(x)^2dx$$

in addition to a change of variable $\omega|\mathbf{r}_m-\mathbf{r}| = x$. This yields

$$\begin{aligned}&\int_{\omega_1}^{\omega_S}J_0(\omega|\mathbf{r}_m-\mathbf{r}|)^2d\omega\\ =&\ \frac{1}{|\mathbf{r}_m-\mathbf{r}|}\int_{\omega_1|\mathbf{r}_m-\mathbf{r}|}^{\omega_S|\mathbf{r}_m-\mathbf{r}|}J_0(x)^2dx\\ =&\ \omega_S\Big(J_0(\omega_S|\mathbf{r}_m-\mathbf{r}|)^2+J_1(\omega_S|\mathbf{r}_m-\mathbf{r}|)^2\Big)\\ &-\omega_1\Big(J_0(\omega_1|\mathbf{r}_m-\mathbf{r}|)^2+J_1(\omega_1|\mathbf{r}_m-\mathbf{r}|)^2\Big)+\int_{\omega_1}^{\omega_S}J_1(\omega|\mathbf{r}_m-\mathbf{r}|)^2d\omega.\end{aligned}$$

Now, we consider the upper bound of

$$\Lambda(|\mathbf{r}_m-\mathbf{r}|,\omega_1,\omega_S):=\int_{\omega_1}^{\omega_S} J_1(\omega|\mathbf{r}_m-\mathbf{r}|)^2 d\omega.$$

Note that since $J_1(0)=0$, let us assume that $|\mathbf{r}_m-\mathbf{r}|\neq 0$ and $0<\omega_S|\mathbf{r}_m-\mathbf{r}|\ll\sqrt{2}$. Then applying asymptotic behavior

$$J_\nu(x)\approx\frac{1}{\Gamma(\nu+1)}\left(\frac{x}{2}\right)^\nu$$

and boundedness property $J_\nu(\omega|\mathbf{r}_m-\mathbf{r}|)\le\frac{1}{\sqrt{2}}$ yields

$$\begin{aligned}&\int_{\omega_1}^{\omega_S} J_1(\omega|\mathbf{r}_m-\mathbf{r}|)^2 d\omega\le\frac{1}{\sqrt{2}}\int_{\omega_1}^{\omega_S} J_1(\omega|\mathbf{r}_m-\mathbf{r}|)d\omega\\ =&\ \frac{1}{\sqrt{2}}\int_{\omega_1|\mathbf{r}_m-\mathbf{r}|}^{\omega_S|\mathbf{r}_m-\mathbf{r}|}\frac{J_1(x)}{|\mathbf{r}_m-\mathbf{r}|}dx=\frac{1}{2\sqrt{2}|\mathbf{r}_m-\mathbf{r}|}\int_{\omega_1|\mathbf{r}_m-\mathbf{r}|}^{\omega_S|\mathbf{r}_m-\mathbf{r}|}xdx\\ =&\ \frac{(\omega_S)^2-(\omega_1)^2}{4\sqrt{2}}|\mathbf{r}_m-\mathbf{r}|<\frac{\omega_S}{4\sqrt{2}}\Big(\omega_S|\mathbf{r}_m-\mathbf{r}|\Big)\ll\frac{\omega_S}{4}=O(\omega_S).\end{aligned}$$

Now, assume that ω_S satisfies

$$\omega_S|\mathbf{r}_m-\mathbf{r}|\gg\sqrt{2}\quad\text{i.e.,}\quad|\mathbf{r}_m-\mathbf{r}|\gg\frac{\sqrt{2}}{\omega_S}>0.$$

Then since

$$\int J_1(x)dx=-J_0(x),$$

we can obtain

$$\begin{aligned}&\int_{\omega_1}^{\omega_S} J_1(\omega|\mathbf{r}_m-\mathbf{r}|)d\omega\\ =&\int_{\omega_1|\mathbf{r}_m-\mathbf{r}|}^{\omega_S|\mathbf{r}_m-\mathbf{r}|}\frac{J_1(x)}{|\mathbf{r}_m-\mathbf{r}|}dx\\ =&\ \frac{1}{|\mathbf{r}_m-\mathbf{r}|}\Big(J_0(\omega_1|\mathbf{r}_m-\mathbf{r}|)-J_0(\omega_S|\mathbf{r}_m-\mathbf{r}|)\Big)\le\frac{2}{|\mathbf{r}_m-\mathbf{r}|}\ll\sqrt{2}\omega_S.\end{aligned}$$

Therefore, the term $\Lambda(|\mathbf{r}_m-\mathbf{r}|,\,\omega_1,\,\omega_S)$ can be disregarded because

$$\begin{aligned}&\frac{\omega_S}{\omega_S-\omega_1}\Big(J_0(\omega_S|\mathbf{r}_m-\mathbf{r}|)^2+J_1(\omega_S|\mathbf{r}_m-\mathbf{r}|)^2\Big)\\ &-\frac{\omega_1}{\omega_S-\omega_1}\Big(J_0(\omega_1|\mathbf{r}_m-\mathbf{r}|)^2+J_1(\omega_1|\mathbf{r}_m-\mathbf{r}|)^2\Big)=O(\omega_S)\end{aligned}$$

and $\Lambda(|\mathbf{r}_m-\mathbf{r}|,\omega_1,\omega_S)\ll O(\omega_S)$. Hence we can obtain (12). This completes the proof.

Two-dimensional plot for (12) is shown in Figure 1. This shows that (11) yields better images owing to less oscillation than (10) does so that unexpected artifacts in the plot of $\mathbb{W}(\mathbf{r}; S)$ are mitigated when S is sufficiently large. This result indicates why a multi-frequency based imaging function offers better results than a single-frequency based one.

4. NUMERICAL EXPERIMENTS AND DISCUSSIONS

In this section, we describe the numerical experiments we conducted to validate our analysis. For this purpose, we choose a set of three different small disks Σ_m. The common radii ρ of Σ_m are set to 0.1, and parameters ε_0 and μ_0 are chosen as 1. Locations $\mathbf{r}_m$ of Σ_m are selected as $\mathbf{r}_1 = (0.4,\ 0)$, $\mathbf{r}_2 = (-0.6,\ 0.3)$, and $\mathbf{r}_3 = (0.1,\ -0.5)$. For a given wavelength λ_s, each frequency is selected as $\omega_s = \frac{2\pi}{\lambda_s}$, for $s = 1, 2, \ldots, S$. Note that the test vector $\mathbf{c}$ in (7) is selected as $\mathbf{c} = (5,\ 1,\ 1)^T$ and all the wavelengths λ_s are uniformly distributed in the interval $[\lambda_1,\ \lambda_S]$. The observation directions $\mathbf{d}_p$ are selected as

$$\mathbf{d}_p = \left(\cos\frac{2\pi p}{N}, \sin\frac{2\pi p}{N}\right) \quad \text{for} \quad p = 1, 2, \ldots, N,$$

and the incident directions $\mathbf{d}_q \in \mathfrak{C}^1$ are selected analogously.

In all the examples, scattered field data are computed within the framework of the Foldy-Lax equation [31]. Then, a white Gaussian noise with 10 dB signal-to-noise ratio (SNR) is added to the unperturbed data in order to exhibit the robustness of the proposed algorithm via the MATLAB command *awgn*. In order to obtain the number of nonzero singular values M for each frequency ω_s, a 0.01-threshold scheme is adopted (see [23, 25]). The search domain $\Omega \subset \mathbb{R}^2$ is selected as a square $\Omega = [-1,\ 1] \times [-1,\ 1]$.

Figure 2 shows the map of $\mathbb{W}(\mathbf{r}; 10)$ via the MSR matrix $\mathbb{M}$ for $N = 20$ and $S = 10$ and different frequencies with $\lambda_1 = 0.5$ and $\lambda_S = 0.3$. On the left-hand side of Figure 2, we set the same material properties $\varepsilon_m \equiv 5$ and $\mu_m \equiv 5$, $m = 1, 2, 3$. As expected, locations of Σ_m can be clearly identified. On the right-hand side of Figure 2, we set different material properties $\varepsilon_1 = \mu_1 = 5$, $\varepsilon_2 = \mu_2 = 2$, and $\varepsilon_3 = \mu_3 = 7$. Notice that, if an inclusion has a much smaller value of permittivity and/or permeability than the other, it does not significantly affect the MSR matrix and consequently, difference in amplitude appearing in the map of $\mathbb{W}(\mathbf{r}; 10)$, refer to [19, 20, 24, 25]. Hence, due to the small values of ε_2 and μ_2, the map of $\mathbb{W}(\mathbf{r};\ 10)$ plots a small magnitude at $\mathbf{r}_2 \in \Sigma_2$ but the locations of all Σ_m are well identified.

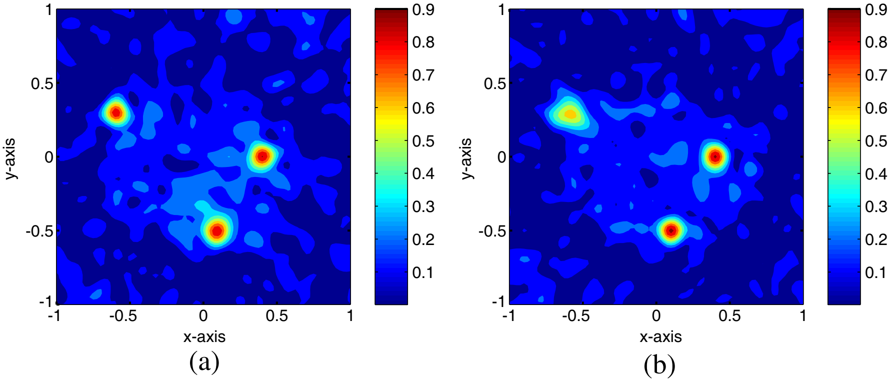

Figure 2. Maps of $\mathbb{W}(\mathbf{r};10)$. (a) Same material property. (b) Different material property.

Figure 3 shows the influence of the number of applied frequencies S. As we discussed in Section 3, increasing S yields a more accurate image. Note that applying an infinite number of S would yield good results in theory, but in this experiment, $S = 10$ is sufficient for obtaining a good result.

Based on the recent work [19], the proposed algorithm can be applied to imaging of extended, crack-like electromagnetic inclusion(s) Γ with a supporting curve γ and a small thickness h. However, note that even a sufficiently large number of N and S applied to obtain a good image of a complex-shaped thin inclusion using the proposed algorithm can occasionally yield poor results (see Figure 4). Furthermore, note that the elements of $\mathbb{M}$ are expressed as written by

$$F(\mathbf{d}_p,\mathbf{d}_q) \sim \sum_{m=1}^{M}\left[\frac{\varepsilon-\varepsilon_0}{\sqrt{\varepsilon_0\mu_0}}+2\left(\frac{1}{\mu}-\frac{1}{\mu_0}\right)\mathbf{d}_p\cdot\mathbf{t}(\mathbf{r}_m)\mathbf{d}_q\cdot\mathbf{t}(\mathbf{r}_m)\right.$$
$$\left.+2\left(\frac{1}{\mu_0}-\frac{\mu}{\mu_0^2}\right)\mathbf{d}_p\cdot\mathbf{n}(\mathbf{r}_m)\mathbf{d}_q\cdot\mathbf{n}(\mathbf{r}_m)\right]\exp\left(jk_0(\mathbf{d}_p+\mathbf{d}_q)\cdot\mathbf{r}_m\right).$$

Therefore, $\mathbf{c}$ in (7) must be a linear combination of a unit tangential vector $\mathbf{t}(\mathbf{r}_m)$ and a normal vector $\mathbf{n}(\mathbf{r}_m)$ at $\mathbf{r}_m \in \gamma$. If we have *a priori* information of $\mathbf{t}(\mathbf{r}_m)$ and $\mathbf{n}(\mathbf{r}_m)$, we can obtain a good result. However, because this is not the case, it is difficult to obtain a good result. This is further explained in detail in [25, Section 4.3.1].

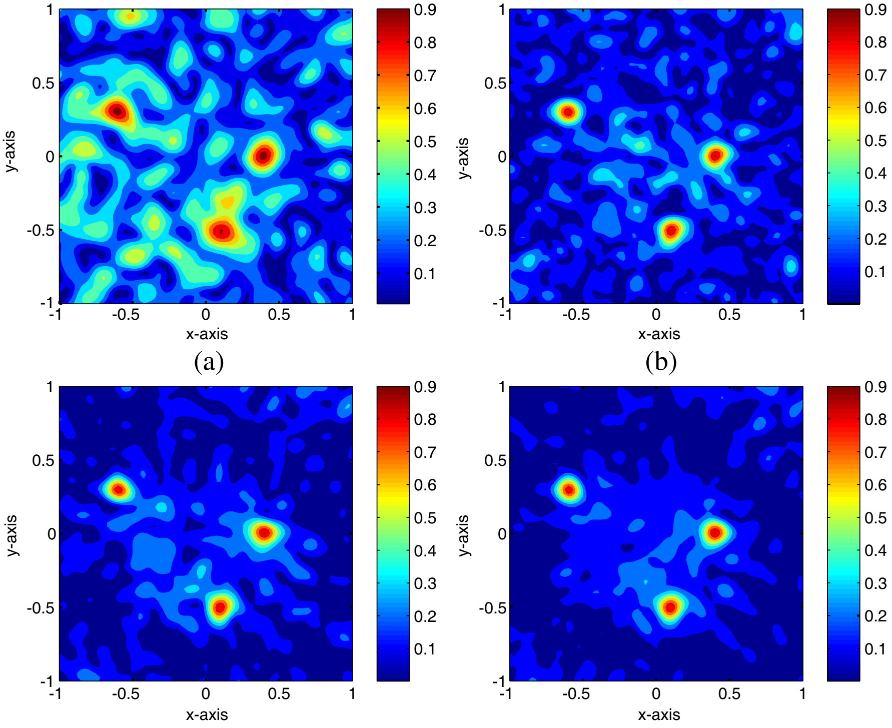

(a) (b)

(c) (d)

Figure 3. Maps of $\mathbb{W}(\mathbf{r}; S)$ with (a) $S = 1$, (b) $S = 3$, (c) $S = 7$, and (d) $S = 20$.

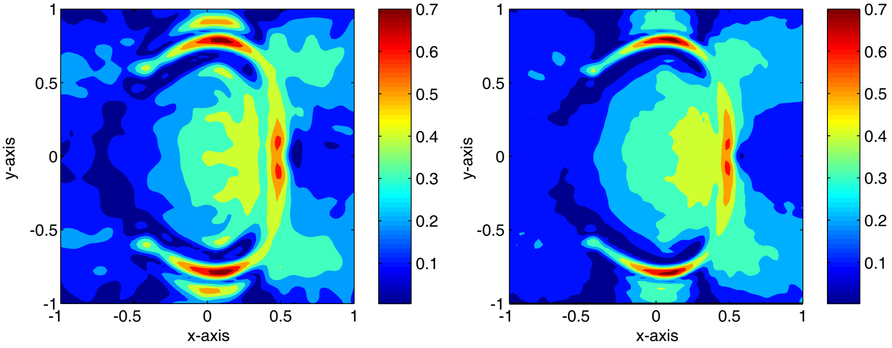

(a) (b)

Figure 4. Maps of $\mathbb{W}(\mathbf{r}; S)$ for complex-shaped thin inclusion. (a) $N = 48$ and $S = 10$. (b) $N = 64$ and $S = 24$.

5. CONCLUSION

Using an integral representation formula and an indefinite integral of the Bessel function, we determined the structure of single and multiple electromagnetic imaging functions. Because of the oscillation aspect of the Bessel function, we confirmed the reason behind the improved imaging performance by successfully applying high and multiple frequencies.

Based on recent works in [4, 6, 19, 20, 24], it has been shown that subspace migration offers better results than the MUSIC and Kirchhoff migration. Specially, subspace migration can be applied to limited-view inverse scattering problems. However, in order to determine the structure of subspace migration in the limited-view problem, the integration in Lemma 3.2 on the subset of a unit circle must be evaluated; however, this evaluation is very difficult to perform. Therefore, identifying the imaging function structure in the limited-view problem will prove to be an interesting research topic. Moreover, in the imaging of crack-like inclusions, estimating unit tangential and normal vectors on such an inclusion and yielding relatively good results will be an interesting work.

Finally, we consider the imaging function for penetrable electromagnetic inclusions, but it will be applied to the perfectly conducting inclusion(s) directly. Extension to the perfectly conducting target will be a forthcoming work. We further believe that the proposed strategy can be extended to a three-dimensional problem. Based on recent work [28], it is confirm that the multi-frequency MUSIC algorithm improves the single-frequency one. Analysis of structure of MUSIC-type algorithm will be the forthcoming work.

ACKNOWLEDGMENT

W.-K. Park would like to thank Habib Ammari for introducing [2] and many valuable advices. The authors would like to acknowledge four anonymous referees for their precious comments. This work was supported by the research program of Kookmin University in Korea, the Basic Science Research Program through the National Research Foundation of Korea (NRF) funded by the Ministry of Education, Science and Technology (No. 2012-0003207), and the WCU (World Class University) program through the National Research Foundation of Korea (NRF) funded by the Ministry of Education, Science and Technology R31-10049.

REFERENCES

1. Álvarez, D., O. Dorn, N. Irishina, and M. Moscoso, "Crack reconstruction using a level-set strategy," *J. Comput. Phys.*, Vol. 228, 5710–5721, 2009.
2. Ammari, H., *Mathematical Modeling in Biomedical Imaging II: Optical, Ultrasound, and Opto-Acoustic Tomographies*, Lecture Notes in Mathematics: Mathematical Biosciences Subseries, Vol. 2035, Springer-Verlag, Berlin, 2011.
3. Ammari, H., J. Garnier, V. Jugnon, and H. Kang, "Stability and resolution analysis for a topological derivative based imaging functional," *SIAM J. Control. Optim.*, Vol. 50, 48–76, 2012.
4. Ammari, H., J. Garnier, H. Kang, W.-K. Park, and K. Sølna, "Imaging schemes for perfectly conducting cracks," *SIAM J. Appl. Math.*, Vol. 71, 68–91, 2011.
5. Ammari, H. and H. Kang, *Reconstruction of Small Inhomogeneities from Boundary Measurements*, Lecture Notes in Mathematics, Vol. 1846, Springer-Verlag, Berlin, 2004.
6. Ammari, H., H. Kang, H. Lee, and W.-K. Park, "Asymptotic imaging of perfectly conducting cracks," *SIAM J. Sci. Comput.*, Vol. 32, 894–922, 2010.
7. Chen, X., "Subspace-based optimization method in electric impedance tomography," *Journal of Electromagnetic Waves and Applications*, Vol. 23, Nos. 11–12, 1397–1406, 2009.
8. Cheney, M., "The linear sampling method and the MUSIC algorithm," *Inverse Problems*, Vol. 17, 591–595, 2001.
9. Delbary, F., K. Erhard, R. Kress, R. Potthast, and J. Schulz, "Inverse electromagnetic scattering in a two-layered medium with an application to mine detection," *Inverse Problems*, Vol. 24, 015002, 2008.
10. Donelli, M., "A rescue radar system for the detection of victims trapped under rubble based on the independent component analysis algorithm," *Progress In Electromagnetic Research M*, Vol. 19, 173–181, 2011.
11. Donelli, M., I. J. Craddock, D. Gibbins, and M. Sarafianou, "A three-dimensional time domain microwave imaging method for breast cancer detection based on an evolutionary algorithm," *Progress In Electromagnetic Research M*, Vol. 18, 179–195, 2011.
12. Colton, D., H. Haddar, and P. Monk, "The linear sampling method for solving the electromagnetic inverse scattering problem," *SIAM J. Sci. Comput.*, Vol. 24, 719–731, 2002.

13. Dorn, O. and D. Lesselier, "Level set methods for inverse scattering," *Inverse Problems*, Vol. 22, R67–R131, 2006.
14. Griesmaier, R., "Multi-frequency orthogonality sampling for inverse obstacle scattering problems," *Inverse Problems*, Vol. 27, 085005, 2011.
15. Hou, S., K. Huang, K. Sølna, and H. Zhao, "A phase and space coherent direct imaging method," *J. Acoust. Soc. Am.*, Vol. 125, 227–238, 2009.
16. Kwon, O., J. K. Seo, and J.-R. Yoon, "A real-time algorithm for the location search of discontinuous conductivities with one measurement," *Commun. Pur. Appl. Math.*, Vol. 55, 1–29, 2002.
17. Lesselier, D. and B. Duchene, "Buried, 2-D penetrable objects illuminated by line sources: FFT-based iterative computations of the anomalous field," *Progress In Electromagnetic Research*, Vol. 5, 351–389, 1991.
18. Ma, Y.-K., P.-S. Kim, and W.-K. Park, "Analysis of topological derivative function for a fast electromagnetic imaging of perfectly conducing cracks," *Progress In Electromagnetics Research*, Vol. 122, 311–325, 2012.
19. Park, W.-K., "Non-iterative imaging of thin electromagnetic inclusions from multi-frequency response matrix," *Progress In Electromagnetics Research*, Vol. 106, 225–241, 2010.
20. Park, W.-K., "On the imaging of thin dielectric inclusions buried within a half-space," *Inverse Problems*, Vol. 26, 074008, 2010.
21. Park, W.-K., "On the imaging of thin dielectric inclusions via topological derivative concept," *Progress In Electromagnetics Research*, Vol. 110, 237–252, 2010.
22. Park, W.-K., "Topological derivative strategy for one-step iteration imaging of arbitrary shaped thin, curve-like electromagnetic inclusions," *J. Comput. Phys.*, Vol. 231, 1426–1439, 2012.
23. Park, W.-K. and D. Lesselier, "Electromagnetic MUSIC-type imaging of perfectly conducting, arc-like cracks at single frequency," *J. Comput. Phys.*, Vol. 228, 8093–8111, 2009.
24. Park, W.-K. and D. Lesselier, "Fast electromagnetic imaging of thin inclusions in half-space affected by random scatterers," *Waves Random Complex Media*, Vol. 22, 3–23, 2012.
25. Park, W.-K. and D. Lesselier, "MUSIC-type imaging of a thin penetrable inclusion from its far-field multi-static response matrix," *Inverse Problems*, Vol. 25, 075002, 2009.
26. Park, W.-K. and D. Lesselier, "Reconstruction of thin electromagnetic inclusions by a level set method," *Inverse Problems*, Vol. 25,

085010, 2009.

27. Rosenheinrich, W., “Tables of some indefinite integrals of bessel functions,” Available at http://www.fh-jena.de/ rsh/Forschung/ Stoer/besint.pdf.
28. Solimene, R., A. Dell’Aversano, and G. Leone, “Interferometric time reversal music for small scatterer localization,” *Progress In Electromagnetics Research*, Vol. 131, 243–258, 2012.
29. Solimene, R., A. Buonanno, and R. Pierri, “Imaging small PEC spheres by a linear delta-approach,” *IEEE Trans. on Eosci. Remote*, Vol. 46, 3010–3018, 2008.
30. Solimene, R., A. Buonanno, F. Soldovieri, and R. Pierri, “Physical optics imaging of 3D PEC objects: Vector and multipolarized approaches,” *IEEE Trans. on Eosci. Remote*, Vol. 48, 1799–1808, 2010.
31. Tsang, L., J. A. Kong, K.-H. Ding, and C. O. Ao, *Scattering of Electromagnetic Waves: Numerical Simulations*, Wiley, New York, 2001.
32. Zhu, G. K. and M. Popovic, “Comparison of radar and thermoacoustic technique in microwave breast imaging,” *Progress In Electromagnetics Research B*, Vol. 35, 1–14, 2011.